

Auto-Crosslinked Rigid Foams Derived from Biorefinery Byproducts

Pierluigi Tosi,^[a] Gerard P. M. van Klink,^[b] Alain Celzard,^[c] Vanessa Fierro,^[c] Luc Vincent,^[a] Ed de Jong,^[b] and Alice Mija^{*[a]}

A new macroporous foam-like material is presented based on autocross-linking humins, an industrial biorefinery byproduct. Humins foams are obtained by a simple heating process, without any pretreatment and with high control of morphology, porosity, and carbon content. Untreated humins have been characterized by GC, ultra-performance liquid chromatography (UPLC), elemental analysis, and FTIR, whereas the mechanism of foaming was elucidated by a combination of thermal and rheological analyses. A preliminary screening of conditions was

conducted to identify the parameters controlling this foaming process. A foam was produced in a controlled way with open and/or closed cells with cell diameters between 0.2 and 3.5 mm. Humins foams were characterized by Raman spectroscopy, FTIR, SEM, nitrogen adsorption, pycnometry, and mechanical tests. The results show that, based on humins, it is possible to obtain porous materials with controlled architectures and a range of parameters that can be tailored, depending on the foreseen applications.

Introduction

Porous materials have a number of key applications such as in catalysis,^[1,2] separation,^[3] sensors,^[4] or ion exchange.^[5] Depending on the expected applications, the important parameters, apart from the IUPAC classification of pore size, are, for example, the effective and apparent porosity, the specific surface area, and the cell morphology. A distinction can also be made between open and closed cells, whether the internal area of each cell is accessible or not. In particular, porous carbon materials derived from sustainable precursors have been shown to have important applications, although these are rather limited to micro-mesoporous activated carbons (ACs) at the industrial scale.^[6,7] Purely mesoporous carbon materials are generally achieved by sacrificial templating followed by high temperatures of carbonization. Thus far, a few studies have been con-

ducted^[7–12] to achieve highly porous functional carbon materials from renewable precursors. This research topic is rapidly growing, attracting interest thanks to the clear economic advantage, the more sustainable chemistry, and the broad range of possible applications. Despite this, important drawbacks have been reported in the synthesis of biomass-based materials, mainly related to the poor control of some key characteristics such as batch-to-batch reproducibility, morphology, porosity, uniformity, surface chemistry, along with the disadvantageous use of toxic chemicals that still might be required. Therefore, biomass precursors that would be both repeatable and easy to use, as well as requiring cost-effective and sustainable synthesis routes, would be most welcome.

Humins

Renewable resources and low-cost biomass in particular have attracted considerable interest during the last few decades as valid alternatives to the massive use of fossil resources. Among them, lignocellulosic biomass represents an appealing option, as it is one of the most abundant carbon sources available in nature.^[13–16] Sugars can be obtained from lignocellulosic biomass^[17] and subsequently converted by biorefinery methods into several platform chemicals. Industrially relevant compounds are 5-hydroxymethylfurfural (HMF) and levulinic acid (LA), derived from the acid-catalyzed dehydration (ACD) of fructose and/or glucose obtained from lignocellulosic biomass.^[18] Unavoidably, during the ACD process, a large amount of insoluble polymeric byproducts called humins are also formed (Scheme 1).^[19–26] Humins are dark-colored highly viscous polymeric materials,^[27] mainly derived from random and uncontrollable condensations of HMF, its precursors, and its derivatives in acidic catalytic conditions. Despite several at-

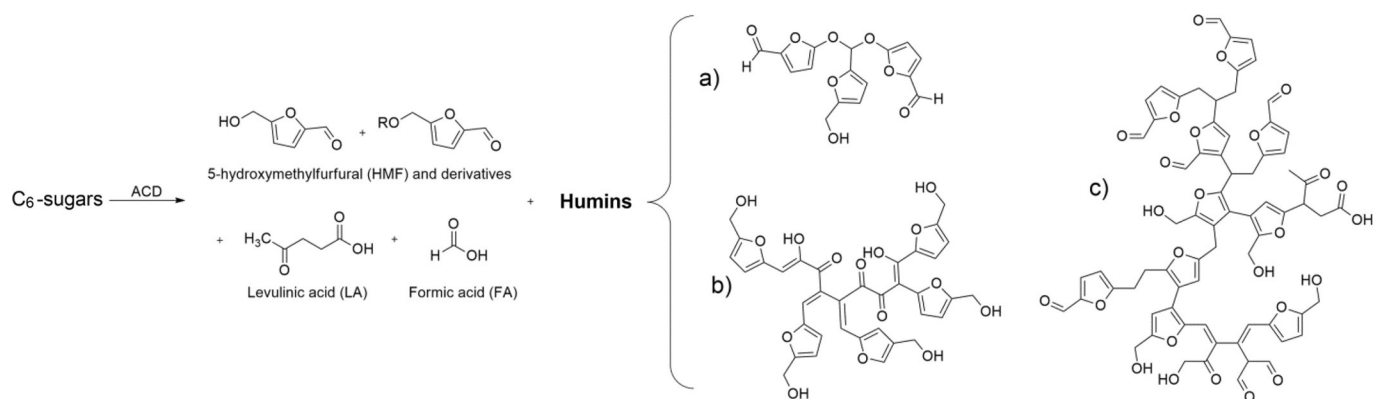
[a] P. Tosi, Dr. L. Vincent, Prof. A. Mija
Institute of Chemistry of Nice, UMR CNRS 7272
Université Côte d'Azur, University of Nice Sophia Antipolis
Parc Valrose, 06108 Nice cedex 2 (France)
E-mail: alice.mija@unice.fr

[b] Dr. G. P. M. van Klink, Dr. E. de Jong
Avantium Chemicals B.V.
Zekeringstraat 29, 1014 BV Amsterdam (The Netherlands)

[c] Prof. A. Celzard, Prof. V. Fierro
Institut Jean Lamour
University of Lorraine
27 rue Ph. Seguin, BP 21042, 88051 Epinal cedex 9 (France)

Supporting Information and the ORCID identification number(s) for the author(s) of this article can be found under:
<https://doi.org/10.1002/cssc.201800778>.

© 2018 The Authors. Published by Wiley-VCH Verlag GmbH & Co. KGaA. This is an open access article under the terms of the Creative Commons Attribution Non-Commercial NoDerivs License, which permits use and distribution in any medium, provided the original work is properly cited, the use is non-commercial and no modifications or adaptations are made.



Scheme 1. Products of acid-catalyzed dehydration of sugars.^[18] Examples of humins structures proposed by a) Sumerskii et al.,^[28] b) Patil and Lund,^[30] and c) Van Zandvoort et al.^[33,34]

tempts at preventing the formation of humins, their production can never be avoided and represents the main drawback for an industrial-scale ACD step. In terms of molecular structure, humins are influenced by the operational conditions used during the ACD process of sugars (e.g., the natures of the solvent, feedstock, and catalyst used, sugar concentrations, temperature, residence time, post-treatment). Therefore, these recalcitrant organic materials are rather ill-defined and their structure is still under investigation. Sumerskii et al.^[28] proposed a pathway for humins formation involving HMF polycondensation through electrophilic substitution, leading to the formation of ether and acetal bonds between the furanic rings. The analysis of the molecular structures of ACD-derived humins revealed a content of 60% furan rings and 20% aliphatic chains. Patil and Lund^[29,30] proposed a mechanism involving the formation of a 2,5-dioxo-6-hydroxyhexanal (DHH) intermediate from the rehydration of HMF. According to this mechanism, DHH leads to aldol condensation with HMF carbonyls. Still, DHH was never detected or isolated, perhaps owing to its high reactivity, but the aldol condensation path was confirmed by addition of benzaldehyde to an HMF solution subjected to ACD reaction. Benzaldehyde was, as expected, included in the humins molecular structure and observed by IR spectroscopy. LA, instead, generally does not seem to be incorporated in the humins network, although IR analysis revealed a conjugated C=C network of aliphatic fragments and furan rings, as well as the presence of carbonyl moieties. In 2017, Constant et al.^[31] quantified for the first time the amount of carbonyl groups in industrial humins, both conjugated and aliphatic, to be 6.6 wt%. Recently, Cheng et al.^[32] identified the electron donor–acceptor-type interaction of humins fragments, indicating that a significant fraction of humins are actually made up by agglomerate of oligomers interacting by weak forces rather than real macromolecules.

Currently, most characterization studies of humins-like materials are based on products prepared by hydrothermal carbonization (HTC),^[8,35] which is a widely employed approach for the production of new carbonaceous materials. Unlike the ACD industrial processes, HTC consists of a hydrothermal treatment of carbohydrates in non-acidic conditions, and therefore the resultant humins are expected to be different.^[36–38] Nonethe-

less, characterization and insight into HTC derivatives can lead to valuable information, as similar conditions are involved and the products can be more easily isolated and purified from the reaction medium.^[39] When using carbohydrates in low-temperature HTC, several soluble products can be produced, mainly furanics (HMF, methoxymethylfurfural (MMF), and furfural), as well as phenols derived from the dehydration of sugars and organic soluble products (e.g., lactic acid, acetic acid, formic acid, and LA).^[37,40] These species undergo polycondensation reactions with different kinetics, leading to humins. Humins can also be obtained directly from the HMF feed in HTC treatment. Sevilla and Fuertes^[36,37] observed in the Raman spectra of HTC-derived humins signals at 1360 and 1587 cm^{−1}, attributed to the D and G bands of disordered carbon. Similar conclusions for the molecular structure of HTC-derived humins were obtained by Yao et al. who studied the dehydration products of fructose.^[41] The Raman spectra showed the presence of aromatic groups and oxygen-rich fragments, along with the D and G bands. An alternative molecular structure was suggested by the Titirici and Baccile group^[42,43] through studies of humins derived from C₅- and C₆-sugars. In this model, furan-rich fragments are directly linked together by aliphatic groups at the α and β positions, whereas LA is physically embedded in the network. Van Zandvoort et al.^[33,34] suggested a mechanism based on condensation between sugars, HMF, and other intermediates formed during the dehydration of carbohydrates, yielding a network of furanic rings bearing alcohol, ketone, aldehyde, and acid moieties. The condensation of HMF occurs with linkages in the α position and substitution in the β position through nucleophilic attack. An NMR analysis^[34] recently provided evidence for C_α–C_{aliphatic} and C_α–C_α bonds in glucose-derived humins. Also, C_β–C_{aliphatic} and C_β–C_β linkages were found in smaller amounts. According to infrared spectroscopy (IR) investigations reported in the literature, HMF-, fructose-, and glucose-derived HTC-humins, generated from different reaction conditions, have similar spectra.^[34,44] However, Tsilomelekis et al.^[45] performed a deeper investigation, showing the evolution of the molecular structure as a function of HMF conversion, and confirmed the involvement of nucleophilic attack of the HMF carbonyl moiety at the α- or β-furanic position. Therefore, according to these results, humins can be considered as

carbonaceous C=C conjugated networks based on furan rings, connected by branched aliphatic chains, and possessing reactive functional oxygen-based groups.

However, humins generated at the industrial scale are definitely more complicated than a collection of ideal pure humins molecules, and should rather be considered as complex mixtures. Along with humins oligomers, other chemicals that were present in the reaction medium during the ACD industrial process are indeed entrapped in the matrix (i.e., solvents, products, byproducts, and catalyst), thus leading to much more complex and heterogeneous materials. On the other hand, purifying such byproducts before their actual use as a feedstock is not desirable as it requires time, is frequently not achievable, and economically not feasible at the industrial level. As a feedstock of growing interest, industrial humins are attracting the interest of the scientific community, and recently several studies have been conducted to modify their structure or identify potential applications.^[25,46,47]

Here, a new approach for humins application is introduced, which does not require any modification or isolation, and which can be directly applied to the industrial crude material. Taking advantage of the hydroxyl, aldehyde, ketone, and acid groups, we oriented our research to achieve auto-cross-linking reactions leading to a thermoset porous material.^[48] It is shown that, by using a simple thermal treatment, it is indeed possible to obtain porous thermosets with tunable properties, just starting from crude industrial humins. These humins foams are porous tailored structures that might play an important role in future applications in well-defined fields such as water decontamination and energy,^[49] which is a clear economic advantage for a biorefinery byproduct.

Results and Discussion

Analysis of humins samples

Using the crude industrial ACD-derived humins mixture, that is, without difficult and expensive purification steps, might be the key to developing economically interesting industrial applications.

To better understand the composition, reproducibility, and reactivity–property relationships, several industrial humins samples prepared by various processing conditions have been subjected to chromatographic investigations by gas chromatography (GC) and ultra-performance liquid chromatography (UPLC). As presented in Table 1, the amount of 5-alkoxymethyl

Table 1. GC and UPLC analysis of six representative industrial humins samples.

Sample	RMF [%]	LA [%]
H1	14.13	1.19
H2	12.35	1.49
H3	13.00	1.40
H4	12.59	1.41
H5	16.43	1.68
H6	11.50	1.25

furaldehydes (RMF), including HMF and MMF (whether encapsulated or reactively generated), was found to be between 11.5 and 16.5 wt%. Other peaks were also found by UPLC, but all were estimated to be below 1 wt%, and therefore are not reported here. The LA content in the humins mixture was found by GC analysis to be less than 2 wt%. Also, methyl levulinate (ML) was generally detected, but its amount was below 0.05%.

Elemental analyses were performed on six samples, and the results are reported in Table 2. The main elements present in crude humins were carbon, oxygen, and hydrogen, although other elements may be present in trace amounts. Such traces could come from the industrial processes that led to humins formation or from the source of lignocellulosic biomass, and were generally estimated to be below 1 wt%. The C amount varied from 53.4 to 57.7% for the tested samples, whereas H was found in the range 5.2–5.9%, and O was close to 40%.

Table 2. Elemental analysis of six representative industrial humins samples.

Sample	C [%]	H [%]	O [%]	Other [%]
H1	57.71	5.25	35.7	1.34
H2	53.48	5.87	40	0.65
H3	53.59	5.88	40.2	0.33
H4	54.61	5.74	39.5	0.15
H5	53.91	5.76	39.8	0.53
H6	53.43	5.89	39.7	0.98

According to these results, the composition of the humins can slightly change depending on the sample. These low variations can be associated with optimizations in the industrial ACD process in terms of temperatures and solvents used, feedstocks, residence time, or concentrations of reagents. The differences in chemical composition are probably not significant, as all the experiments of auto-cross-linking and foaming performed on the six samples gave very similar results. This observation can be associated with the fact that, independently of the sample tested, the phenomena leading to the foam production are always present with consistent results.^[48] Therefore, we chose to focus the crude humins characterization only on the H6 sample, as it was the most readily available.

Fourier transform infrared spectroscopy (FTIR) analyses were performed to detect the modifications in the humins' chemical structure during the auto-cross-linking, depending on the thermodynamic parameters of reaction. In the raw humins, the presence of -OH groups is evident from a peak at 3350 cm⁻¹, with a broad shape indicative of hydrogen bonds, as presented in Figure 1 and in Table 3. Carbonyls can be found in particular at 1705 and 1664 cm⁻¹, mainly associated with humins macromolecules and partly with free unbounded monomers (such as HMF, MMF, and LA). These carbonyls can belong to several functionalities (aldehydes, ketones, esters, acids), as confirmed by the variety of peaks. The presence of furanic rings can be noticed by several signals in the entire spectrum (Table 3). Typical peaks associated with HMF can be found at 1190 and 1664 cm⁻¹, whereas the presence of ethers can be attributed

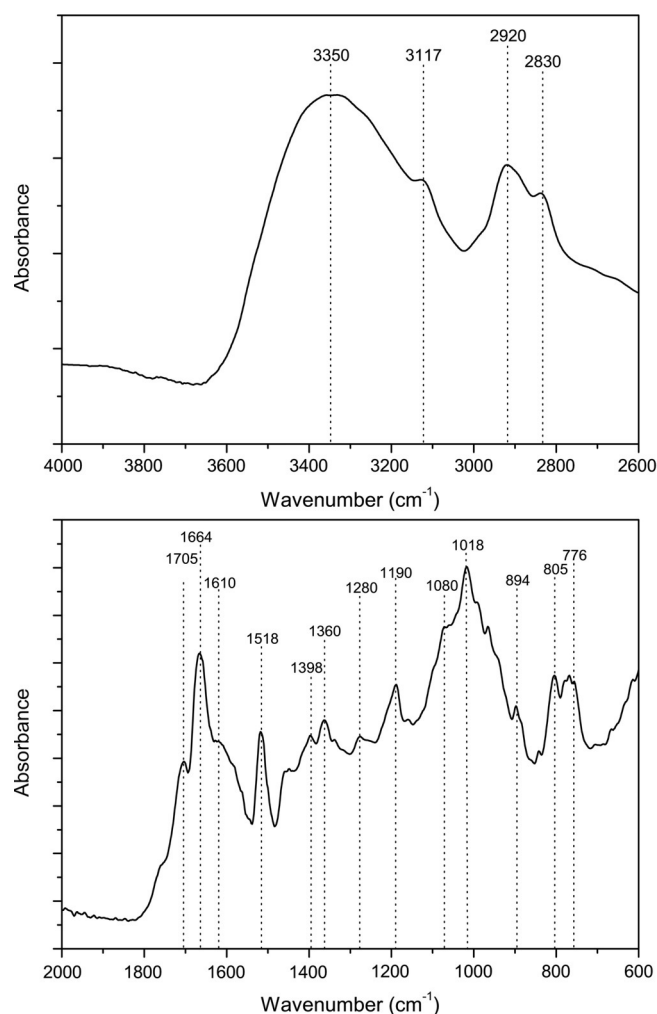


Figure 1. FTIR spectra of crude humins.

Table 3. Peaks assignments for FTIR spectrum of crude humins.	
Wavenumber [cm ⁻¹]	Assignment
3350	—OH
3117	(C=C)—H
3920	C—H (sp ³)
2830	C=C
1705	conjugates C=O, COO, esters
1664	C=O, furan ring
1610, 1518	C=C, C=O, furan rings
1398	C=C in ring
1360	C—O
1280–1110	C—O, C—O—C
1190, 805, 776	furan ring
1080	(ethers, esters, furans)
1018	C—O (furan ring)
894	α-CH ₃ and α-CH ₂
850–760	=C—H, =CH ₂ , RCH=CHR (<i>cis</i>), C—H

by peaks in the 1300–960 cm⁻¹ region. Most detected groups correspond to highly reactive moieties, which justify the thermosetting aptitude of humins through cross-linking and condensation reactions.

Assessment of auto-cross-linking and foaming mechanisms

A polymeric foam can be produced from any polymer, provided that the three following aspects are met: the polymer is in a low-viscosity state, gas is released, and there is concomitant hardening of the material during the formation of bubbles.^[50] According to this generalization, achieving foaming requires a poorly viscous material (in the molten state or as an unreacted mixture) that is able to solidify during a physicochemical treatment (by cross-linking), while the key factor is the formation and release of a gas accompanying the process.

As the thermal events in crude humins are hardly seen by differential scanning calorimetry (DSC), rheometric analysis was used as proof that auto-cross-linking occurs during the heating program. The evolution of the complex viscosity of humins upon heating up to 200 °C is shown in Figure 2. The first criti-

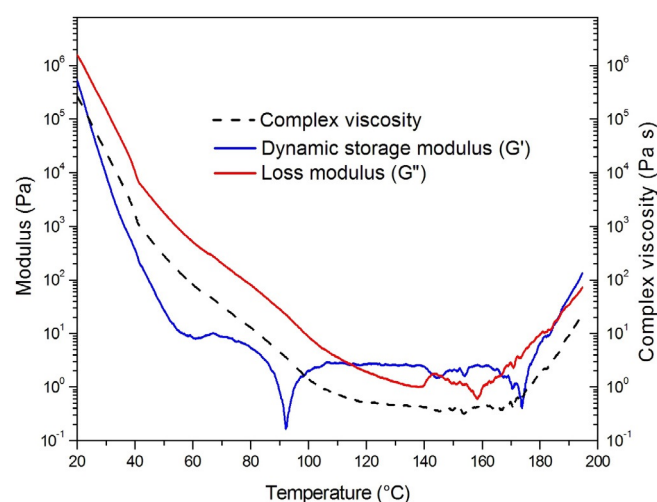


Figure 2. Rheometry analysis of crude humins.

cal range of temperatures is between 20 and 125 °C, as the humins' viscosity drops by approximately 2.5×10^5 Pa s. At 125 °C, the humins' viscosity reaches a value as low as approximately 0.48 Pa s, characteristic of a liquid state. Above 140 °C, fluctuations in the rheogram appear owing to the onset of volatiles release, as observed by optical microscopy during heating. From then on, the changes of moduli are chaotic, and only trends are exploitable. The increase of viscosity starting at 170 °C can be associated with the initiation of auto-cross-linking reactions by internal condensations. For the H6-humins sample, this temperature is the critical point in the process of condensation and curing, where volatiles are being generated from the sample bulk, setting the necessary conditions to obtain foams. These thermal phenomena are subject to some small shifts in temperature (± 5 °C) when the same tests are performed on different humins samples (H1–H5). However, the aforementioned, successive, phenomena were always detected, and therefore the overall mechanism was confirmed for the whole series of samples tested.

The dynamic storage modulus (G') and the loss modulus (G'') were plotted as functions of temperature to extract infor-

mation about changes in the sample's viscoelastic state (Figure 2). G' measures the energy that a material stores per cycle and can be associated with the elastic contribution, whereas G'' measures the energy dissipated or lost, and can be associated with the viscous contribution.^[51] The phenomenon recorded on G' and localized at around 93 °C is relative to some evaporation of adsorbed water, leading to a mass loss lower than 0.3%, as confirmed by thermogravimetric analysis coupled with mass spectroscopy (TGA-MS; Figure 4). It should be mentioned that this water cannot be removed by high-vacuum treatment at moderate temperatures, nor by prolonged heat-treatments; hence, this phenomenon should be taken into account also for the following tests. A first G'/G'' crossover point was detected at 114.5 °C, and can be associated with the initiation of condensation reactions. The recorded fluctuations of G' and G'' above 140 °C are associated with gas release, leading to bubbling at around 169 °C. A gelation point is present at around 186 °C, triggering the formation of a giant macromolecular chain spanning the complete sample volume. Once initiated, cross-linking and condensation reactions continued and the hardening process became irreversible.

According to DSC analysis, pristine crude humins presented a midpoint for the T_g at -15 °C, whereas in foams F250 (derived from humins, details in the Experiment Section), it was found at 66 °C, proving that the thermal treatment generates reticulation and cross-linking reactions (Figure S1 in the Supporting Information). The T_g occurs in a wide range of temperatures (≈ 40 °C in raw humins, > 100 °C in foams), which is clearly due to the heterogeneous nature of these materials.

Thermogravimetric analysis shows the thermal behavior of humins and the mass loss associated with this heating process, along with information about the gases involved in the bubbling that lead to the resultant macroporosity. A TGA comparison of H6 humins samples under air and N_2 is reported in Figure 3. In both environments, a first mass loss of 38–39% occurred between 140 and 260 °C, with a maximum at 210–220 °C. This event can be assigned to the release of low-molecular-mass species present in the humins composition or pro-

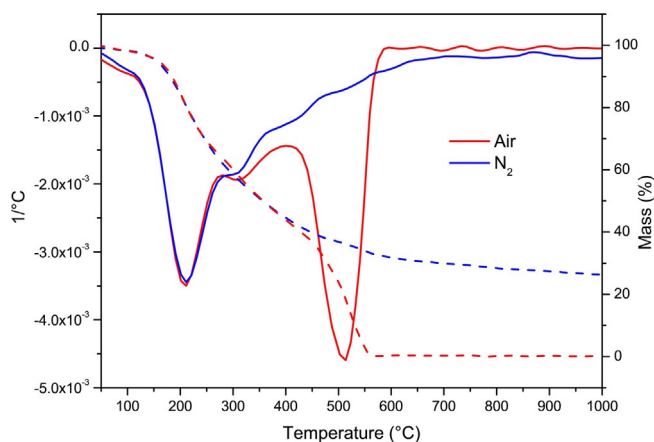


Figure 3. Thermogravimetric analysis comparison of H6 humins under air and under N_2 : relative weight loss in % (dashed lines); derivative weight loss in $1/^\circ\text{C}$ (full lines).

duced by condensation reactions. The polymerization between the chain fragments may also have occurred in this temperature interval. This is the range of temperatures characterizing the foaming process, and therefore the gases released here were those directly implied in the nucleation of bubbles. The second event occurred between 280 and 340 °C, and corresponds to a mass loss of 19–20% under air and of less than 10% under nitrogen. The final event occurred only in air, up to 415 °C. It is related to the thermo-oxidative degradation of humins and led to the complete gasification of the sample at 560 °C. On the other hand, the thermogram under nitrogen showed that, at 1000 °C, approximately 26–27% of the residue was still present. This value is only slightly lower than that of pure furfuryl alcohol submitted to pyrolysis under argon ($\approx 40\%$).^[52]

To identify the species released during these mass loss steps, humins samples were subjected to investigation by TGA-MS under Ar (Figure 4). The first phenomenon started at

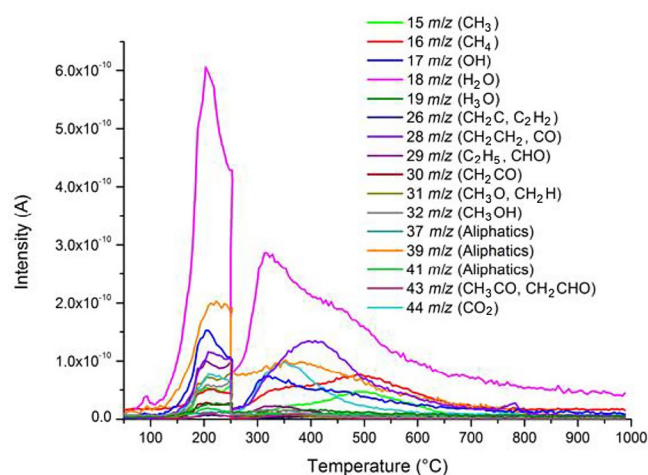


Figure 4. TGA-MS analysis of crude humins under Ar. Thermal program: heating from 25 to 250 °C at 5°C min^{-1} ; 1 h isothermal step at 250 °C; heating from 250 to 1000 °C at 5°C min^{-1} . Gas: Ar, 50 mL min^{-1} .

150 °C with a maximum at 203 °C, and is due to the combination of several peaks of mass loss related to different species. CO and MeOH were detected along with CO_2 , but the principal volatile species was water. Water can be released as a byproduct in condensation reactions (such as aldol condensation), leading to losses in oxygenated functional groups. A second mass loss started at 275 °C with a maximum at 315–340 °C and is again associated with water loss, with a contribution of CO_2 loss, which had its maximum peak at 350 °C. Finally, a third mass loss step was detected with a maximum peak at 400–420 °C and was mainly associated with CO release. CH_4 was also detected with a peak at 500 °C, which overlapped the previous one.

Foaming of humins

To identify which parameters govern the foaming process of crude humins under air, a preliminary screening with more

than 70 experimental conditions was performed. The foams were evaluated in terms of reproducibility, homogeneity, morphology (cell dimensions), density, porosity, mechanical properties, and proportion of open/closed cells as a function of the humins sample used, amount of material used, type and dimensions of the crucible, heating ramp, gas flow, and other relevant aspects (Table S1 in the Supporting Information).

In general, when a lower amount of humins was used, foams with smaller pores and higher homogeneity were obtained. Comparing the results obtained by using different crucibles, porcelain generally gave smaller pores and denser foams. Aluminum pans, on the other hand, tended to give foams with bigger pores and lower density.

Clearly, the thermal program is of first importance as, depending on: i) final temperature, ii) dynamic and/or isothermal heating, and iii) heating rate, completely different cell morphologies can be obtained. The duration of the isothermal step at the final temperature, however, did not seem to influence the final material morphology.

Among all the thermal programs investigated, a $10^{\circ}\text{C min}^{-1}$ ramp generally led to more reproducible and uniform outcomes. All the samples tested gave comparable results, after previous slight optimization of the parameters. As we chose to continue the screening on one single sample, the H6 humins, which was the most readily available, all the foam preparation conditions and characterizations reported herein again refer to this sample.

Three experimental conditions/temperatures were found to be extremely reproducible for foaming humins in an oven under air (Table 4). Experiment "A" for foam F180 provided a

creased the viscosity, so that bubble generation tended to be more controlled.

Experiment "C" led to the formation of foam F250 with big and uniform cells (diameters up to 3 mm). This material looked more fragile compared with other experiments because of its bigger pores, providing lower density and thinner cell walls. Unlike the previous experiment, here half of the cells were open, while the closed ones had extremely thin walls/membranes.

Other protocols gave less uniform foams and less reproducible porous structures, which are nevertheless interesting and worth being studied. Completely open cells were obtained at temperatures higher than 300°C . Treatments at 400°C , depending on the conditions, could lead to thermo-oxidative degradations (as indicated also by TGA experiments on crude humins), until complete gasification. When recovered, the obtained residual material presented a loss of cell walls, yielding a completely open porous structure. The temperature, in these cases, seems to consume first the thin cell walls and then the thicker parts of the foam (ligaments and junctions).

Foams were also prepared at higher temperatures by using a tubular furnace flushed with N_2 , that is, in an inert environment. F500 and F900 were found to be less homogeneous compared with the foams prepared at lower temperatures, with a complex morphology and a fully open structure.

A post-treatment at 900°C was also tested for F250. As previously mentioned, the protocol "C" used for F250 gave really homogeneous foams with big cells, among which roughly half were closed by thin polymeric membranes. The idea was to check if an additional carbonization step, inducing the expected significant weight loss seen in Figure 3 between 250 and 900°C , would produce a completely open structure by preferentially degrading the thinner parts of the foam. After this post-treatment, a porous networked material with fully open structure was indeed obtained (Figure 5). In these F250-900 materials, all the cell walls were lost, leaving only a honeycomb-like skeleton. Unlike F400, F250-900 presented a thicker architecture, meaning that the temperature affected only the cells' surface and not the bulk of the structure.

Table 4. Best three conditions out of more than 70 tested to achieve highly reproducible foams under air. In all the experiments, 1 h isothermal step at the final temperature was used.

Experiment	Heating rate [$^{\circ}\text{C min}^{-1}$]	Final T [$^{\circ}\text{C}$]	Crucible material	Crude humins [g]	Pore diameter [mm]	
					min.	max.
A	10	180	ceramic	50	0.4–1.3 ^[a]	2.4–3.5 ^[a]
B	10	220	ceramic	50	0.2	1
C	10	250	aluminum	23	1.1	3

[a] A gradient was observed.

vertical gradient of cell sizes. The cells were closed, and their diameter increased from the top (0.4–1.3 mm) to bottom (2.4–3.5 mm). The same gradients were also reported for tannin-based foams, which are other cellular materials derived from biomass.^[53] Experiment "B" led to F220: uniform foams with closed cells and lower cell diameter (0.2–1 mm). Compared with experiment "A", the vertical gradient was absent in experiment "B". This can be explained as follows: as bubbling started at $\approx 175^{\circ}\text{C}$, a progressive and moderate bubbling probably occurred in experiment "A" (180°C). In experiment "B" (220°C), that is, far above this critical point, a diffusive homogeneous bubbling was generated. Furthermore, as reported in the rheological analyses, the higher temperature of experiment "B" in-

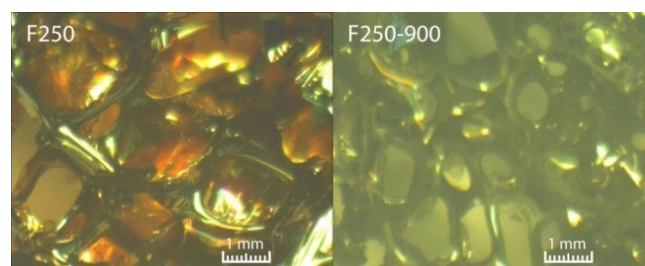


Figure 5. Morphology of foams F250 before (left) and after (right) post-treatment at 900°C .

Foam characterization

Elemental analysis

Elemental analysis of different foams presented in Table 5 shows that, as expected, the O/C ratio decreased with an increase in the final temperature. According to these results, the carbon content rose from 53.43% in crude humins to 81.92% in F400.

Table 5. Comparison of elemental analysis for humins and humins foams prepared with different thermal programs.				
Sample	C [%]	H [%]	O [%]	Other [%]
crude	53.43	5.89	39.7	0.98
F200	59.08	5.12	34.4	1.40
F250	63.12	4.52	30.9	1.46
F300	67.65	3.86	27.6	0.89
F400	81.92	3.03	13.8	1.25
F900	92.56	0.80	4.59	2.05
F250-900	94.48	0.52	1.85	3.15

in F400, while the H and O percentages decreased accordingly (Table 5). This is due to furanics rearrangement, volatiles loss, degradation, and aromatization, which occur at higher temperature, consistent with the literature reports for polyfuranic carbonization.^[54] The oxygen content decreased from 39.7% in the crude humins to 13.8% in F400. This means that oxygen reactive moieties were mainly reduced but not completely lost at 400 °C, as already observed elsewhere for heat-treated phenolic-furanic foams.^[55]

As shown in Table 5, F900 is a true carbonaceous material, as its carbon content was as high as 92.56%. The residual hydrogen amount, <1%, can be associated with an almost complete aromatization of the structure.

The highest carbon content was found for F250-900 (94.48%). The hydrogen ratio dropped to about 0.5%, whereas oxygen remained at a level <2%. The double thermal treat-

ment thus seemed to favor the loss of reactive moieties and to enhance the aromatization.

As observed in the Van Krevelen diagram (Figure 6), the H/C and O/C atomic ratios were linearly related to each other. Depending on the foreseen applications, it is therefore possible to design the composition, especially the carbon content, by controlling the thermal program during auto-cross-linking and foaming processes.

Structural characterization

Auto-crosslinked humins foams prepared at different temperatures were characterized by FTIR, and the results were compared with the crude humins spectrum (Figure 7). The signal at 3350 cm⁻¹ shifted to 3421 cm⁻¹ and progressively decreased in intensity when the temperature of preparation increased, showing a diminution of hydroxyls in the structure. The shifting of this signal can be related to the increase of the conjugated C=C system. The signal at 2920 cm⁻¹, associated with ali-

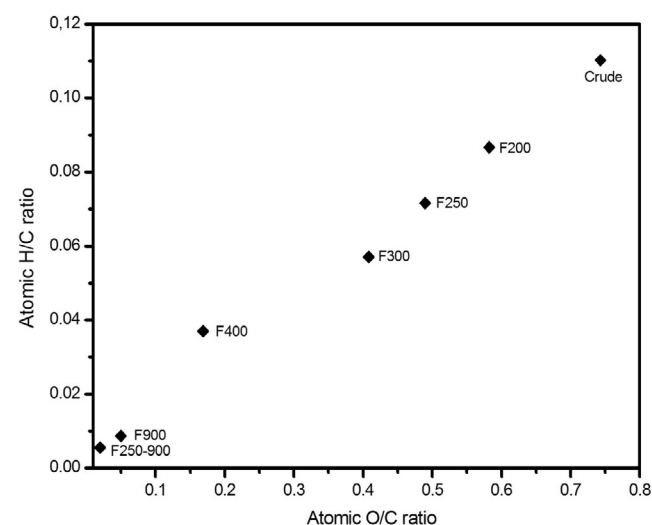


Figure 6. Van Krevelen diagram for humins foams.

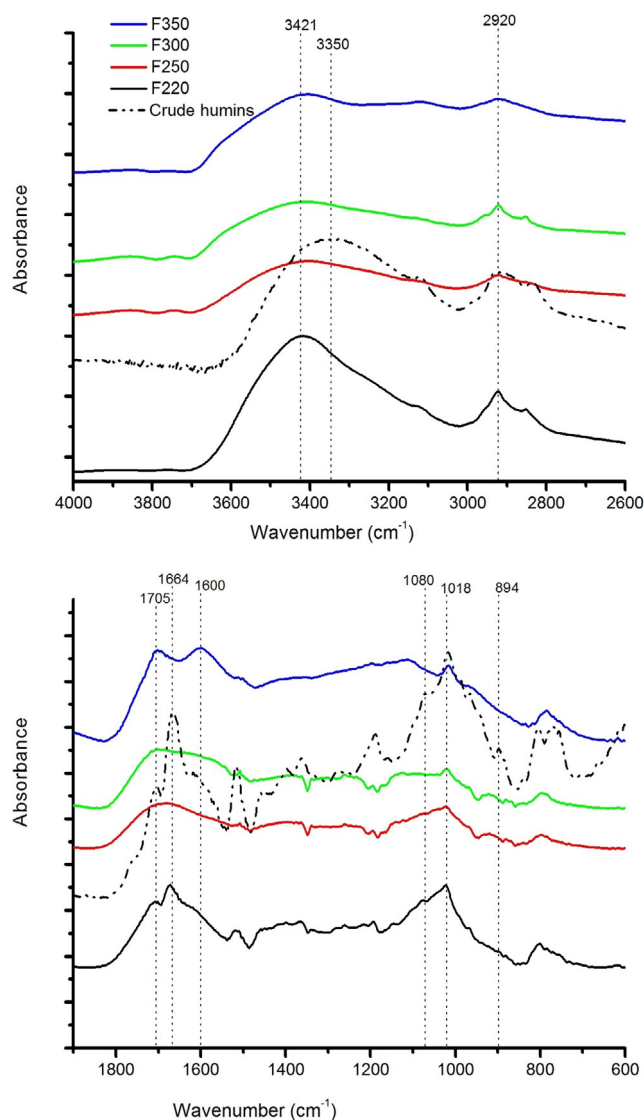


Figure 7. FTIR of auto-crosslinked humins foams.

phatic C–H stretching, was still detected. It is worth noticing that the peak at 1664 cm^{-1} related to CO groups was still present in F220, but disappeared from F250. On the other hand, the peak at 1705 cm^{-1} , which was barely visible in the IR spectra of crude humins, herein clearly appeared in F220 and became the main signal up to 250°C . This signal can be associated with CO groups within conjugated systems, and its increase confirms that reactions of aromatization and rearrangement occurred. Also, a new signal appeared at 1600 cm^{-1} in F350, and can be associated with poly-aromatic formation.

The thermal treatment manifested most of its effects in the furanic region at $1460\text{--}1362\text{ cm}^{-1}$, in which the vanishing of peaks suggests ring rearrangement. In addition, the loss of the signal at 1080 cm^{-1} is correlated with the release of CO found by TGA-MS, which confirms the breaking of furan ether ring functions. The signal at 1018 cm^{-1} assigned to $\alpha\text{-CH}_3$ and $\alpha\text{-CH}_2$ bending was maintained, whereas the peak at 894 cm^{-1} disappeared. The latter can be ascribed to $=\text{C-H}$ and $=\text{CH}_2$ out-of-plane bending, and this disappearance might be linked to rearrangements and aromatization, which involve firstly the external chains, or rearrangement from *cis* to *trans* double bonds (the less energetic stereoisomer). Observed changes in the region $850\text{--}760\text{ cm}^{-1}$ may correspond to ring rearrangements and hydroxyls loss owing to reactions of condensation through nucleophilic attack.

Raman spectra of F300 and F900 foams are compared in Figure 8. The spectrum of F300 is typical of a carbonaceous material in the carbonization regime (and not in the graphitization regime), as it presents the classic D and G bands at 1360 cm^{-1} and 1590 cm^{-1} , respectively, but with a broad contour and with G being much more intense than D.^[56] The D band (1360 cm^{-1}) is well known in complex carbon-based materials and is associated with a breathing mode of A_{1g} symmetry of the carbon rings. In highly disordered carbons, another broad band, less intense and centered around 1180 cm^{-1} overlaps the D band, as also seen here by a shoulder at about 1200 cm^{-1} . This is characteristic of soot or coal chars,^[57–59] but

the interpretation of this signal is still under investigation.^[60,61] The G band (1590 cm^{-1}), instead, corresponds to a Raman active vibrational $2E_{2g}$ mode of graphite single crystals, and can be associated with the degree of metallicity of the structure.

These two peaks were also detected for F900, with the D band slightly shifted to 1345 cm^{-1} , which is perhaps due to the effect of the sp^2/sp^3 carbon peripheral polyenes. The Raman peak intensity height ratio I_D/I_G changed from approximately 0.75 in F300 to about 1 in F900. Such behavior in the carbonization regime is characteristic of increased long-range order in the carbonaceous structure. This is related to a higher average crystallite size of sp^2 carbon domains, owing to the higher carbon amount and higher aromatization of F900.^[62] This is important proof of the extension of the conjugated system in reticulated porous networks treated at high temperature under inert gas.

Scanning electron microscopy (SEM) and Brunauer–Emmett–Teller (BET) method

To investigate the foam morphologies, SEM images were collected for F250, F500, and F900, and are reported in Figure 9. In F250, well-defined spherical cells with a smooth surface can be observed (Figure 9, F250 A). The cells were connected to each other through some circular windows, making the macropores completely open and interconnected (Figure 9, F250 C and F250 D). However, in some cases, the windows were not completely open but closed by thin, somewhat wrinkled, membranes (Figure 9, F250 E). The materials of the F250 foam looked solid, and no additional porosity could be observed at such magnification (Figure 9, F250 F). This lack of narrow porosity gives its structure to the foam backbone and makes it strong. In both F500 and F900, a loss of regularity in the morphology could be noticed, the resultant structure being affected by degradation and cracking of cell walls and architecture (Figure 9, F500 A and F900 A). In F900 also, microcracks appeared, which increased the surface area of the material. It is also possible to see that, whereas F500 did not clearly present a secondary porosity (Figure 9, F500 C), a number of tiny holes could be seen at the surface of F900 (Figure 9, F900 C). This result was confirmed by BET results (Table 6), and is consistent with the continuous release of volatiles produced at higher temperature whereas the carbonaceous structure shrinks and rigidifies at the same time, thereby developing the porosity. Similar results were also obtained by Burket et al.^[54] for the pyrolysis of polyfurfuryl alcohol: these researchers observed that with thermal treatments micro- and mesoporosity are obtained. In this case, the effect was associated with the formation of polyaromatic domains and with the release of decomposition products.

According to BET analysis (Table 6), the surface area of F250 is about $0.2\text{ m}^2\text{ g}^{-1}$, representing a highly macroporous system. This value rose to $2.3\text{ m}^2\text{ g}^{-1}$ with treatment at 500°C , and up to $74.4\text{ m}^2\text{ g}^{-1}$ with treatment at 900°C . The foam prepared at 250°C and post-treated at 900°C even reached almost $140\text{ m}^2\text{ g}^{-1}$. This confirms the production of additional pores in

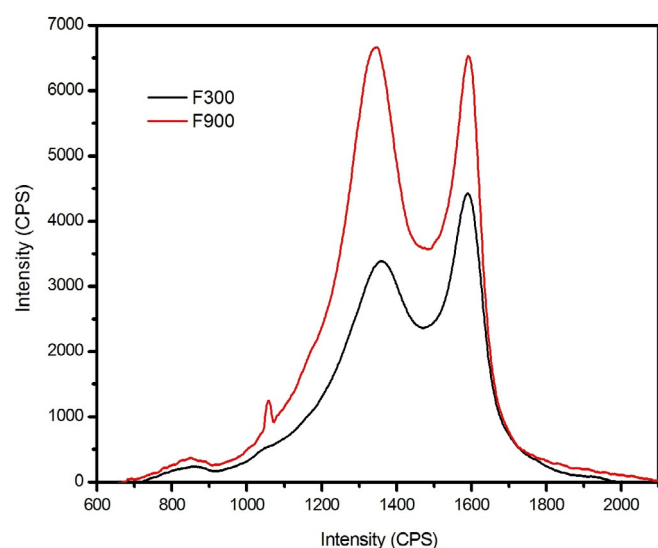


Figure 8. Raman spectra of humins foams F300 and F900.

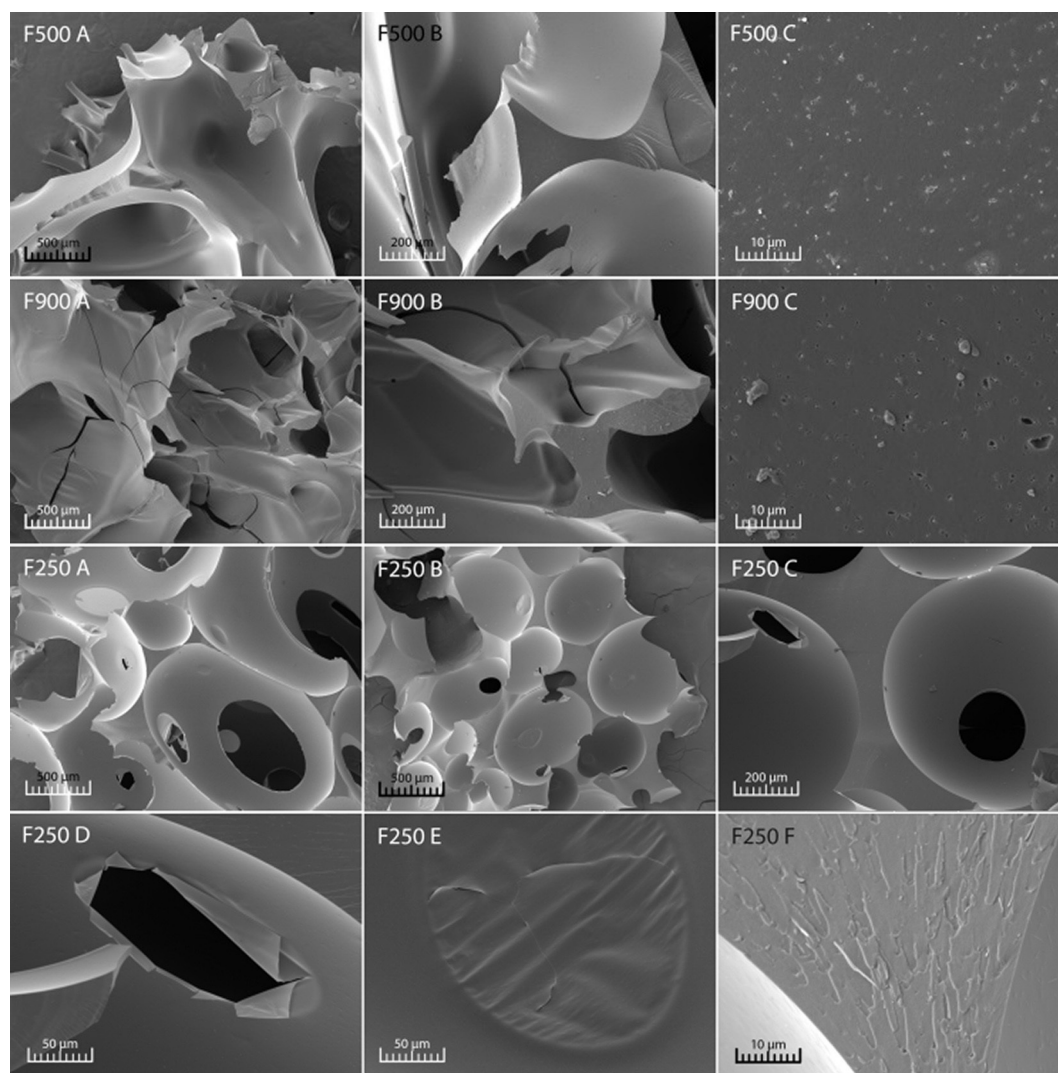


Figure 9. SEM images for F250, F500, and F900 foams at different magnifications.

Table 6. BET results for several humins foams.	
Sample	BET surface area [$\text{m}^2 \text{g}^{-1}$]
F250	0.2
F500	2.3
F900	74.4
F250-900	138.9

F900, as displayed in Figure 9 (F900 D). Considering that this result was obtained with a single hour of final isothermal treatment at 900°C , and that a secondary porous network was thus created, the material might be easily converted into a monolithic activated carbon by heat-treatment in a flow of CO_2 steam, for instance, for reaching far higher surface areas.

Porosity and Apparent and real density

As seen in Table 7, the apparent density (ρ_{apparent}) of foams F180–F250 prepared in air significantly decreased when the

temperature of preparation increased. This is due to the fact that higher temperatures produced bigger cells and hence a more lightweight material, as also shown by the corresponding increase of porosity (Φ). On the other hand, the real density (ρ_{real}) of these foams remained unaffected as the difference of temperature used ($\Delta T = 70^\circ\text{C}$) was not high enough to justify significant structural changes. F500 and F900 did not follow this trend because of the very different temperature or treatment: ρ_{apparent} increased from 0.046 to 0.069 g cm^{-3} , whereas

Table 7. Apparent, real, and relative density as well as porosity of humins-derived foams.				
Sample	ρ_{apparent} [g cm^{-3}]	ρ_{real} [g cm^{-3}]	ρ_{relative}	Φ [%]
F180	0.132	1.402	0.094	90.58
F220	0.045	1.407	0.032	96.80
F250	0.020	1.403	0.014	98.58
F500	0.046	1.437	0.032	96.77
F900	0.069	1.985	0.035	96.52

ρ_{real} increased from 1.437 to 1.985 g cm⁻³ owing to the pyrolysis at 900 °C. As a result, the relative density (ρ_{relative}) was roughly constant. This is related to the dramatic shrinkage of the foam submitted to pyrolysis under inert atmosphere, and to the conversion of the furanic resin into a disordered carbon material, the specific weight of which was expected to be close to 2 g cm⁻³. Weight loss and volume shrinkage thus compensated almost exactly, leaving the final porosity quite high and comparable to what was obtained when using lower temperatures in air.

Mechanical properties

The results presented in Table 8 show that humins foams prepared under air are quite fragile materials, given their low Young's moduli and compressive strengths. Clearly, far better mechanical properties were obtained after pyrolysis at 900 °C (F900) owing to the intrinsic stiffness of glass-like isotropic carbon derived from furanic resins.

Table 8. Young's modulus E and compressive stress σ of humins foams.

Sample	E [MPa]	σ [MPa]
F180	0.60	0.006
F250	0.52	0.011
F900	12.23	0.123

Although these properties remain limited, humins foams might find applications where mechanical resistance is not critical, for instance, in most energy and environmental applications for which materials are used in the form of powders. Getting foams is indeed a very convenient preliminary step before the surface area and the narrow porosity can be developed further. Highly porous carbons derived from humins foams might be quite relevant as catalyst supports, adsorbents, or electrode materials. More demanding applications such as core materials for (thermal or acoustic) insulating panels would require some changes in the formulation and/or the thermal treatment, but are out the scope of the present paper. For instance, much tougher foams were already obtained by reinforcing them with natural fibers.^[48]

Conclusions

As byproducts from the industrial acid-catalyzed dehydration of sugars, humins proved to be excellent precursors for producing new rigid porous materials. Their intrinsic self-foaming and auto-cross-linking ability above 180 °C, without any pre-treatment, was highlighted. The underpinning mechanism of humins foaming was identified as a combination of phenomena: melting at 120 °C, release of volatiles (mainly H₂O, CH₃OH, CO, and CO₂) above 140 °C, auto-cross-linking above 170 °C, and gelation at around 186 °C. From this point, bubbles were stabilized in the thermoset humins-based resin, leading to the cellular structure of the final material.

Auto-cross-linking is possible by the presence of several reactive oxygen moieties such as hydroxyls and carbonyls, which can be involved in aldol condensation, along with reactions of rearrangements and furan condensation. Indeed, FTIR showed that -OH groups were progressively lost when increasing the foams' preparation temperature, whereas CO groups were more and more involved in the conjugated systems. New peaks appeared with temperature, associated with furanic rearrangement and aromatization.

Humins foams could be obtained with high control of morphology and cell dimensions by adjusting the parameters used during their preparation process. Foams prepared at low temperatures (between 180 and 250 °C) were quite homogeneous in terms of size and shape of the cells, the latter being mainly closed. Foams prepared at higher temperatures (350–900 °C) were gradually less homogeneous, with a more open porosity, until only a reticulated structure remained. Higher temperatures of treatment increased the surface area and produced a secondary porosity, and could be converted into true vitreous carbon foams at 900 °C under inert atmosphere. In addition, pyrolysis considerably improved the mechanical properties of the materials, and opened the routes towards environmental and energy applications, such as catalyst supports, absorbents, or electrode materials. This will be the subject of forthcoming studies.

Experimental Section

Six crude humins samples were provided by Avantium Chemicals, which were produced by using different times/protocols at the Avantium pilot plant in Geleen (Netherlands) in 2016 during ACD of fructose and glucose into MMF. The ACD conversion of hexoses into MMF is a key step in the production of 2,5-FDCA (2,5-furandicarboxylic acid) for the formation of polyethylene furanoate (PEF). The as-produced humins were then distilled under high vacuum to remove most of the HMF and MMF content, and then used as received. These humins oligomers have molecular masses that generally range from 270 to 650 g mol⁻¹.^[46]

Humins foams preparation

All humins foams described herein were prepared from crude humins by using the following thermal program: heating from room temperature (r.t.) to final temperature at 10 °C min⁻¹; isotherm = 1 h. After the process, the samples were allowed to cool down to r.t. Foam samples were named "F" followed by the final temperature used (e.g., F250 was prepared by using 250 °C as the final temperature).

F180, F200, F220, F250, F300, F350, and F400 were prepared in air in Nabertherm K430/75 and Nabertherm N30/85HA ovens, by using Haldenwanger Evaporating Basin Porcelain Flat 888/6A, LLG-Incinerating Dish and disposable aluminum pans as crucibles.

F500 and F900 were prepared under inert atmosphere (flowing N₂, 80 mL min⁻¹) in a Carbolite CTF 12/100/900 Tube Oven furnace, by using a LLG-Incinerating Dish.

F250–900 was prepared from F250 by using a second temperature program until 900 °C under N₂.

Chromatography

An external standard solution (ESS) was first prepared by dissolving saccharine (8 g L^{-1}) and dioxane (3 g L^{-1}) in acetonitrile (MeCN). A sample for GC was then prepared by dissolving humins in 4 mL ESS + 2 mL water (if required, an ultrasonic bath was used to fully dissolve the sample). Another sample for UPLC was prepared from 20 μL GC sample + 800 μL water + 180 μL MeCN.

GC analyses were performed with an Interscience Trace GC device, equipped with a FID detector and VF WAXms column, id 0.25 mm, film thickness 0.25 μm , 30 m. Eluent: MeCN/ H_2O 50:50; injection volume: 1 μL . Dioxane was used as the standard for both calibration and samples.

UPLC analyses were performed with a Waters Acquity UPLC HSS C18 column, $2.1 \times 100 \text{ mm}$, 1.8 μm . Eluent: 0.2% trifluoroacetic acid in H_2O and MeCN/MeOH 50:50. Injection volume: 3.5 μL ; flow: 0.4 mL min^{-1} ; internal standard: saccharine (measured at 250 nm). Column temperature: 50 $^\circ\text{C}$, equipped with UV and ELSD detectors. MMF and HMF contents were detected by UPLC-UV analysis.

Thermal analysis

TGA was performed by using a Mettler Toledo TGA/SDTD 851, with a microbalance precision of $\pm 0.1 \mu\text{g}$. The data were treated with STAR \odot software. Humins and humins foams (10–15 mg) were investigated in 70 μL alumina pans as crucibles. Humins foams were crushed before analysis to obtain homogeneous powder samples. The investigations were performed by using dynamic thermal programs from 25 to 1000 $^\circ\text{C}$ at a heating rate of 10 $^\circ\text{C min}^{-1}$ and under air or nitrogen flow (50 mL min^{-1}).

TGA-MS studies were performed with a Netzsch STA449F3 thermobalance coupled to an Aëolos QMS403D mass spectrometer equipped with a quadrupole analyzer. Crude humins samples of approximately 20 mg were heated under inert gas (Ar, 50 mL min^{-1}) in alumina pans from 25 to 1000 $^\circ\text{C}$ at 5 $^\circ\text{C min}^{-1}$ with an isothermal plateau of 1 h at 250 $^\circ\text{C}$. The transfer line was heated at 250 $^\circ\text{C}$ and maintained under vacuum (1×10^{-9} – 1×10^{-8} bar). The gases were analyzed in the range 1–300 amu. Peaks associated with flowing Ar ($m/z=40$, 38, and 36) were removed from the spectra.

DSC studies on crude and foamed humins were conducted with a Mettler-Toledo DSC-1 equipped with FRS5 sensor and monitored by STAR \odot software. The calibrations (temperature, enthalpy) were performed by using indium and zinc standards. Samples of 7–11 mg were placed in 40 μL aluminum crucibles with sealed lids pierced by a single hole. The same crucibles were used as references. Humins foams were crushed before analysis. The experiments for detecting the temperature range of T_g were conducted between –60 and 125 $^\circ\text{C}$ for crude humins and between –60 and –300 $^\circ\text{C}$ for humins foams, with a 30 $^\circ\text{C min}^{-1}$ ramp in both cases.

Rheology

Rheological characterization of crude humins was performed with a Thermo Scientific HAAKE MARS Modular Advanced Rheometer System operated with a plate–plate geometry (1 mm gap). Experimental conditions were: sample weight $\approx 10 \text{ g}$; temperature range from 0 to 200 $^\circ\text{C}$ at 1 $^\circ\text{C min}^{-1}$; 5% deformation, oscillation frequency 1 Hz.

Raman spectroscopy

Raman spectra of two samples of humins foams (F300 and F900) were acquired at room temperature by using a DXR Raman Microscope AXX1606015 series, with laser depolarized at wavelength 532 nm, grating 900 lines mm^{-1} , split aperture 25 μm ; acquisition time of exposition 0.25 s, number of expositions 120.

Pycnometry

Four different humins foams prepared in ceramic crucibles were characterized in terms of ρ_{apparent} , ρ_{real} , and Φ . ρ_{apparent} was calculated as the weight/volume ratio of foams shaped like parallelepipeds of accurately known dimensions. ρ_{real} or skeletal density, being the density of the solid material constituting the foam, was estimated by helium pycnometry after grinding the sample, using an Accupyc II 1340 (Micromeritics, USA) apparatus. From the two aforementioned quantities, ρ_{relative} was defined as the ratio of ρ_{apparent} to ρ_{real} . The overall porosity (dimensionless), was calculated as $\Phi = 1 - \rho_{\text{relative}}$. The measurements were performed on parallelepiped samples of humins foams of typical size around $3 \times 3 \times 1.5 \text{ cm}$, cut out of bigger foam blocks.

Mechanical tests

The mechanical properties of humins thermoset foams prepared in ceramic crucibles were investigated by quasi-static compression by using an Instron 5944 universal testing machine equipped with a 2 kN head, and using a load rate of 2.0 mm min^{-1} . Three samples of dimensions approximately $3 \times 3 \times 1.5 \text{ cm}$ were tested in the growing direction for each formulation. Owing to their brittle character, the opposite faces of parallelepiped sample of the same material were glued to poly(methyl methacrylate) (PMMA) plates with a high-resistance epoxy adhesive (Araldite) before testing, according to a described method.^[63] During the test, deformation and load were continuously recorded: the modulus was estimated from the slope of the longest linear region at strain typically lower than 10%, and the compressive strength was defined as the highest stress before densification.^[64,65]

FTIR

FTIR analyses were performed with a PerkinElmer Spectrum BX FTIR System (range 4000–600 cm^{-1} , 32 scans, resolution 4 cm^{-1} , interval 2 cm^{-1}). All the spectra were treated with baseline automatic correction and smoothing. Crude humins samples were analyzed by using attenuated total reflection (ATR) mode. Humins foams were analyzed based on the ground material mixed with KBr ($\approx 2:100$) to obtain sufficient signal intensity.

Elemental analysis

Crude humins elemental analyses were performed with inductively coupled plasma (ICP) by Mikroanalytisches Labor Pascher, Remagen, Germany.

SEM

SEM observations of F250, F500, and F900 were carried with a Tescan Vega3 XM scanning electron microscope. Prior to observation, samples were cut and coated with platinum. A 5 kV accelerating voltage was used for imaging.

Nitrogen adsorption

The humins foams surface area was estimated by using a TriStar 3000 device from Micromeritics serial #470. The surface area was calculated by the regression line in the BET transform plot of nitrogen adsorption at -196°C of crushed samples, according to the BET model equations.^[66] Prior to analysis, the samples were dried at 200°C under a N_2 stream.

Acknowledgements

The authors would like to acknowledge the European Commission for financial support: H2020 MSCA project "HUGS", GA 675325. Special thanks go to François Orange for his help and assistance with SEM observations performed at CCMA Common Center of Applied Electronic Microscopy of University of Nice Sophia Antipolis, and to Koen Kramer from Avantium Chemicals for the BET analysis. We warmly thank Stephane Le Bras from Thermofisher Scientific for Raman analysis and Clara Delgado-Sanchez from IUL for some foams characterization.

Conflict of interest

The authors declare no conflict of interest.

Keywords: cross-linking • biorefinery • carbonaceous materials • humins • rigid foams

- [1] R. Haag, S. Roller, *Immobilized Catalysts: Solid Phases, Immobilization and Applications*, Springer, Berlin, **2004**.
- [2] S. De, A. M. Balu, J. C. Van Der Waal, R. Luque, *ChemCatChem* **2015**, *7*, 1608–1629.
- [3] M. Slater, M. Snauko, F. Svec, J. M. J. Fréchet, *Anal. Chem.* **2006**, *78*, 4969–4975.
- [4] D. Wang, F. Li, M. Liu, G. Q. Lu, H. Cheng, *Angew. Chem. Int. Ed.* **2008**, *47*, 373–376; *Angew. Chem.* **2008**, *120*, 379–382.
- [5] K. A. Kun, R. Kunin, *J. Polym. Sci. C* **1967**, *16*, 1457–1469.
- [6] R. J. White, R. Luque, V. L. Budarin, J. H. Clark, D. J. Macquarrie, *Chem. Soc. Rev.* **2009**, *38*, 481–494.
- [7] B. Hu, K. Wang, L. Wu, S. H. Yu, M. Antonietti, M. M. Titirici, *Adv. Mater.* **2010**, *22*, 813–828.
- [8] M. M. Titirici, A. Thomas, S. H. Yu, J. O. Müller, M. Antonietti, *Chem. Mater.* **2007**, *19*, 4205–4212.
- [9] A. Sanchez-Sanchez, M. T. Izquierdo, J. Ghanbaja, G. Medjahdi, S. Mathieu, A. Celzard, V. Fierro, *J. Power Sources* **2017**, *344*, 15–24.
- [10] A. Sanchez-Sanchez, M. T. Izquierdo, S. Mathieu, J. González-Álvarez, A. Celzard, V. Fierro, *Green Chem.* **2017**, *19*, 2653–2665.
- [11] J. Encalada, K. Savaram, N. A. Travlou, W. Li, Q. Li, C. Delgado-Sánchez, V. Fierro, A. Celzard, H. He, T. J. Bandoz, *ACS Catal.* **2017**, *7*, 7466–7478.
- [12] G. Xu, J. Han, B. Ding, P. Nie, J. Pan, H. Dou, H. Li, X. Zhang, *Green Chem.* **2015**, *17*, 1668–1674.
- [13] A. E. Farrell, R. J. Plevin, B. T. Turner, A. D. Jones, M. O'Hare, D. M. Kammen, *Science* **2006**, *311*, 506–508.
- [14] M. Galbe, G. Zacchi, *Appl. Microbiol. Biotechnol.* **2002**, *59*, 618–628.
- [15] D. J. Hayes, *Catal. Today* **2009**, *145*, 138–151.
- [16] M. Mascal, E. B. Nikitin, *Angew. Chem. Int. Ed.* **2008**, *47*, 7924–7926; *Angew. Chem.* **2008**, *120*, 8042–8044.
- [17] S. G. Wettstein, D. Martin Alonso, E. I. Gürbüz, J. A. Dumesic, *Curr. Opin. Chem. Eng.* **2012**, *1*, 218–224.
- [18] R. Van Putten, J. C. Van Der Waal, E. De Jong, C. B. Rasrendra, H. J. Heeres, J. G. De Vries, R.-J. van Putten, J. C. van der Waal, E. de Jong, C. B. Rasrendra, H. J. Heeres, J. G. de Vries, *Chem. Rev.* **2013**, *113*, 1499–1597.
- [19] B. F. M. Kuster, L. M. Tebbens, *Carbohydr. Res.* **1977**, *54*, 158–164.
- [20] B. F. M. Kuster, H. M. G. Temmink, *Carbohydr. Res.* **1977**, *54*, 185–191.
- [21] B. F. M. Kuster, *Carbohydr. Res.* **1977**, *54*, 177–183.
- [22] B. Girisuta, B. Danon, R. Manurung, L. P. B. M. Janssen, H. J. Heeres, *Bioresour. Technol.* **2008**, *99*, 8367–8375.
- [23] B. Girisuta, L. P. B. M. Janssen, H. J. Heeres, *Green Chem.* **2006**, *8*, 701–709.
- [24] B. Girisuta, L. P. B. M. Janssen, H. J. Heeres, *Ind. Eng. Chem. Res.* **2007**, *46*, 1696–1708.
- [25] A. Mija, J. C. Van Der Waal, J. Pin, N. Guigo, E. De Jong, *Constr. Build. Mater.* **2017**, *139*, 594–601.
- [26] L. Filiciotto, G. de Miguel, A. M. Balu, A. A. Romero, J. C. van der Waal, R. Luque, *Chem. Commun.* **2017**, *53*, 7015–7017.
- [27] L. Filiciotto, A. M. Balu, J. C. Van der Waal, R. Luque, *Catal. Today* **2018**, *302*, 2–15.
- [28] I. V. Sumerskii, S. M. Krutov, M. Y. Zarubin, *Russ. J. Appl. Chem.* **2010**, *83*, 320–327.
- [29] S. K. R. Patil, J. Heltzel, C. R. F. Lund, *Energy Fuels* **2012**, *26*, 5281–5293.
- [30] S. K. R. Patil, C. R. F. Lund, *Energy Fuels* **2011**, *25*, 4745–4755.
- [31] S. Constant, C. S. Lancefield, B. M. Weckhuysen, P. C. A. Bruijninx, *ACS Sustainable Chem. Eng.* **2017**, *5*, 965–972.
- [32] Z. Cheng, J. Everhart, G. Tsilomelekis, V. Nikolakis, B. Saha, D. Vlachos, *Green Chem.* **2018**, *20*, 997–1006.
- [33] I. Van Zandvoort, E. J. Koers, M. Weingarth, P. C. A. Bruijninx, M. Baldus, B. M. Weckhuysen, *Green Chem.* **2015**, *17*, 4383–4392.
- [34] I. Van Zandvoort, Y. Wang, C. B. Rasrendra, E. R. H. Van Eck, P. C. A. Bruijninx, H. J. Heeres, B. M. Weckhuysen, *ChemSusChem* **2013**, *6*, 1745–1758.
- [35] M.-M. Titirici, R. J. White, N. Brun, V. L. Budarin, D. S. Su, F. del Monte, J. H. Clark, M. J. MacLachlan, *Chem. Soc. Rev.* **2015**, *44*, 250–290.
- [36] M. Sevilla, A. B. Fuertes, *Carbon* **2009**, *47*, 2281–2289.
- [37] M. Sevilla, A. B. Fuertes, *Chem. Eur. J.* **2009**, *15*, 4195–4203.
- [38] N. Baccile, G. Laurent, F. Babonneau, F. Fayon, M.-M. Titirici, M. Antonietti, *J. Phys. Chem. C* **2009**, *113*, 9644–9654.
- [39] M. M. Titirici, M. Antonietti, *Chem. Soc. Rev.* **2010**, *39*, 103–116.
- [40] T. M. Aida, Y. Sato, M. Watanabe, K. Tajima, T. Nonaka, H. Hattori, K. Arai, *J. Supercrit. Fluids* **2007**, *40*, 381–388.
- [41] C. Yao, Y. Shin, L. Q. Wang, C. F. Windisch, W. D. Samuels, B. W. Arey, C. Wang, W. M. Risen, G. J. Exarhos, *J. Phys. Chem. C* **2007**, *111*, 15141–15145.
- [42] M.-M. Titirici, M. Antonietti, N. Baccile, *Green Chem.* **2008**, *10*, 1204–1212.
- [43] C. Falco, N. Baccile, M.-M. Titirici, *Green Chem.* **2011**, *13*, 3273–3281.
- [44] S. Reiche, N. Kowalew, R. Schlögl, *ChemPhysChem* **2015**, *16*, 579–587.
- [45] G. Tsilomelekis, M. J. Orella, Z. Lin, Z. Cheng, W. Zheng, V. Nikolakis, D. G. Vlachos, *Green Chem.* **2016**, *18*, 1983–1993.
- [46] L. Filiciotto, A. M. Balu, A. A. Romero, E. Rodríguez-Castellón, J. C. van der Waal, R. Luque, *Green Chem.* **2017**, *19*, 4423–4434.
- [47] A. Mija, J. C. van der Waal, E. de Jong, G. van Klink, (Avantium Knowledge Center), WO 2018062995 A1, **2018**.
- [48] A. Mija, E. de Jong, J. C. van der Waal, G. van Klink, (Avantium Knowledge Center), WO 2017074183 A1, **2017**.
- [49] L. Wei, M. Sevilla, A. B. Fuertes, R. Mokaya, G. Yushin, *Adv. Energy Mater.* **2011**, *1*, 356–361.
- [50] G. Tondi, A. Pizzi, *Ind. Crops Prod.* **2009**, *29*, 356–363.
- [51] J. D. Ferry, *Viscoelastic Properties of Polymers*, 3rd ed., Wiley, New York, **1980**.
- [52] A. Shindo, K. Izumino, *Carbon* **1994**, *32*, 1233–1243.
- [53] G. Tondi, W. Zhao, A. Pizzi, G. Du, V. Fierro, A. Celzard, *Bioresour. Technol.* **2009**, *100*, 5162–5169.
- [54] C. L. Burket, R. Rajagopalan, A. P. Marencic, K. Dronvajjala, H. C. Foley, *Carbon* **2006**, *44*, 2957–2963.
- [55] G. Tondi, A. Pizzi, H. Pasch, A. Celzard, K. Rode, *Eur. Polym. J.* **2008**, *44*, 2938–2943.
- [56] S. Bernard, O. Beyssac, K. Benzerara, N. Findling, G. Tzvetkov, G. E. Brown, *Carbon* **2010**, *48*, 2506–2516.
- [57] A. Sadezky, H. Muckenhuber, H. Grothe, R. Niessner, U. Pöschl, *Carbon* **2005**, *43*, 1731–1742.
- [58] T. Livneh, E. Bar-Ziv, O. Senneca, P. Salatino, *Combust. Sci. Technol.* **2000**, *153*, 65–82.
- [59] A. Zaida, E. Bar-Ziv, L. R. Radovic, Y. J. Lee, *Proc. Combust. Inst.* **2007**, *31* II, 1881–1887.

- [60] B. Dippel, H. Jander, J. Heintzenberg, *Phys. Chem. Chem. Phys.* **1999**, *1*, 4707–4712.
- [61] E. Bar-Ziv, A. Zaida, P. Salatino, O. Senneca, *Proc. Combust. Inst.* **2000**, *28*, 2369–2374.
- [62] A. C. Ferrari, J. C. Meyer, V. Scardaci, C. Casiraghi, M. Lazzeri, F. Mauri, S. Piscanec, D. Jiang, K. S. Novoselov, S. Roth, A. K. Geim, *Phys. Rev. Lett.* **2006**, *97*, 187401.
- [63] M. Letellier, C. Delgado-Sanchez, M. Khelifa, V. Fierro, A. Celzard, *Carbon* **2017**, *116*, 562–571.
- [64] A. Celzard, W. Zhao, A. Pizzi, V. Fierro, *Mater. Sci. Eng. A* **2010**, *527*, 4438–4446.
- [65] G. Amaral-Labat, M. Sahimi, A. Pizzi, V. Fierro, A. Celzard, *Phys. Rev. E* **2013**, *87*, 032156.
- [66] P. Webb, C. Orr, *Analytical Methods in Fine Particle Technology*, Micromeritics Instrument Corp, Norcross, GA, USA, **1997**.

Manuscript received: April 10, 2018
 Revised manuscript received: June 26, 2018
 Accepted manuscript online: June 29, 2018
 Version of record online: July 25, 2018
